ELSEVIER

International Journal of Heat and Fluid Flow 21 (2000) 432–441

International Journal of HEAT AND FLUID FLOW

www.elsevier.com/locate/ijhff

A numerical method for simulation of forced convection in a composite porous/fluid system

Baili Zhang [1], Yong Zhao *

School of Mechanical and Production Engineering, Nanyang Technological University, Nanyang Avenue, Singapore 639798, Singapore

Received 19 January 1999; accepted 17 August 1999

Abstract

A new unstructured-grid high-order characteristics upwind finite-volume algorithm for accurate numerical simulation of incompressible laminar flow and forced convection heat transfer over a composite system containing simultaneously porous-saturated region and fluid region is presented in this paper. It is an upwind method at both the differential equation and discretized equation levels based on the method of characteristics. Flow variables are calculated along characteristics and their initial values are interpolated based on the signs of the corresponding characteristic speed. In addition, an upwind-based interpolation method of third-order accuracy is used for interpolating flow variables on an unstructured grid. With these inherent upwind techniques for evaluation of convection fluxes at control volume surfaces, no artificial viscosity is required. The discretized equations are then solved by an explicit multistage Runge–Kutta time stepping scheme together with a point-implicit treatment of the source terms. Unified governing equations for the fluid and porous media regions are employed, and the matching conditions at the fluid–porous interface are thus satisfied automatically. This significantly reduces the complexity of the traditional method, which considers two regions separately. A detailed numerical investigation of fluid flow over a backward-facing step with a porous block insert directly behind the step is performed, in order to validate the numerical method, demonstrate the accuracy and robustness of the scheme proposed and explore the use of porous inserts for heat transfer enhancement in recirculating flow.

Keywords: Heat transfer; Incompressible flow; Convection in porous media

1. Introduction

Theoretical and numerical investigations of fluid flow and forced convection heat transfer in a composite system containing simultaneously fluid region and porous region saturated with the same fluid have increased during recent years. This interest is due to the wide range of engineering applications such as direct contact heat exchangers, heat pipes, electronic cooling, etc. It has been demonstrated that insertion of porous material can have a positive effect on convective heat transfer. Hadim (1994) numerically studied the laminar forced convection in a fully or partially porous channel with discrete heat sources on the bottom wall. Huang and Vafai (1994) reported numerical results for forced convection enhancement in a channel using multiple emplaced porous blocks, and Fu et al. (1996) studied the thermal performance in laminar channel flow with only one porous block later. Abu-Hijleh (1997) investigated flow over a backward-facing step with a porous floor segment. More recently, numerical results for heat transfer enhancement with porous inserts in the recirculation region of a flow over a 2D backward-facing step were presented by Martin et al. (1998).

All above-referred investigations were based on traditional numerical method for incompressible flow simulation on structured grids (Patankar, 1980). Here, a new high-order upwind finite-volume method based on the method of characteristics for calculating incompressible flow over a porous/fluid composite system is presented. The upwind bias is introduced at both the differential equation level and the discretized equation level. Thus it is less sensitive to grid orientation, making it more suitable for unstructured grid application. Traditionally, the method of characteristics is used primarily for compressible flow calculations (Eberle, 1985). However, with the introduction of the pseudo-time derivative of pressure in the continuity equation (Chorin, 1967), it is possible that the incompressible equations can also be solved by a similar method of characteristics. Based on this idea, a high-order upwind characteristics method has been developed for numerical solution of incompressible flow equations on unstructured triangular grids (2D) for convection heat transfer simulation.

* Corresponding author.

E-mail addresses: zhangbl@ihpc.nus.edu.sg (B. Zhang), myzhao@ntu.edu.sg (Y. Zhao).

[1] Present address: Institute of High Performance Computing, 89C Science Park Drive, #02-11/12 The Rutherford, Singapore 118261, Singapore.

0142-727X/00/$ - see front matter
PII: S0142-727X(00)00029-1

Notation

a	length of porous insert
c	specific heat
Da	Darcy number, K/H^2
F	inertial coefficient
$\vec{F}_c$	convective flux vector
$\vec{F}_v$	viscous flux vector
H	channel height
h_l	head loss
k	thermal conductivity
K	permeability of the porous medium
L	channel length
Nu	Nusselt number
Pr	Prandtl number, v_f/α_f
p	pressure
q	heat flux
Re	Reynolds number, $u_{av}H/v_f$
R_k	thermal conductivity ratio, k_{eff}/k_f
S_p	source term due to porous insert
t	time
T	temperature
u, v	velocity components in the x- and y-directions
$\vec{U}$	velocity vector
u_{av}	inlet averaging streamwise velocity
W	vector of dependent variables

Greeks

α	thermal diffusivity
β	artificial compressibility
γ	kinetic energy coefficient
ε	porosity of porous medium
λ	binary parameter
λ^k	wave speed
v	kinetic viscosity
ξ	normal co-ordinate
ρ	density
σ	heat capacity ratio
φ	smoothing coefficient

Superscripts

n	time step counter
$*$	dimensionless quantity

Subscripts

av	average
b	bulk
eff	effective
f	fluid
h	homogeneous
i	inlet
o	outlet
w	wall

It is shown that this method is mathematically simpler and can be easily extended to arbitrary 3D unstructured grids in the finite-volume frame work together with high-order schemes such as MUSCL interpolation. With these inherent upwind techniques for evaluating convection fluxes at control volume surfaces, no artificial viscosity is required. The use of the finite-volume method combined with unstructured grids makes the scheme very flexible in dealing very complex boundary geometry, while maintaining fully conservative at both the cell level as well global level. The discretized equations are solved by a multistage Runge–Kutta time stepping scheme. Combined with point-implicit treatment of the source terms and implicit smoothing of residuals this method is found to be robust and efficient even for stiff problems such as fluid flow in porous media with low Darcy number.

In order to validate the computer code developed and demonstrate the accuracy and robustness of the scheme, a detailed numerical investigation on fluid flow over a 2D backward-facing step with a porous block insert directly behind the step is performed. The result obtained shows that the use of even relatively lower thermal conductive porous insert can improve heat transfer performance greatly.

2. Mathematical model

A schematic of the physical model for a specific porous/fluid composite system is shown in Fig. 1. This diagram displays a 2D incompressible flow over a backward-facing step, the channel is partially filled directly behind the step with a porous matrix insert. It is assumed that the flow is steady, laminar, incompressible, and two-dimensional. The porous medium is considered to be homogeneous, isotropic, and in local thermodynamic equilibrium with saturated fluid. In addition, the thermophysical properties of the fluid and the solid matrix are assumed to be constant.

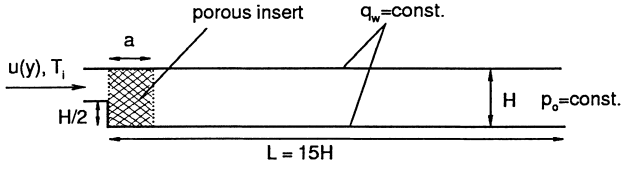

Fig. 1. Schematic of the physical model.

The governing conservation equations for the present problem can then be written separately for the fluid region and porous region. The flow over the fluid region is governed by the incompressible Navier–Stokes equation, and the flow through the porous medium is governed by the generalised momentum equation, which accounts for the effect of the inertia and friction caused by macroscopic shear stress (Vafai and Tien, 1981). In this study, the Brinkman–Forchheimer–Extended Darcy model is used to model the flow inside the porous region. These two sets of equations are coupled through the matching conditions at the fluid/porous interface. These conditions express continuity of normal and tangential velocities, pressure, normal and shear stresses, temperature, and heat flux.

In our present work, the two sets of governing equations are unified into one set by introducing a binary parameter (Hadim, 1994)

$$\lambda = \begin{cases} 1 & \text{in the prous regions, } 0 < \varepsilon < 1, \\ 0 & \text{in the fluid regions, } \varepsilon = 1. \end{cases}$$

In the fully porous channel case or no-porous insert case, λ is set to equal 1 or 0 throughout the channel, respectively. When we solve the derived unified governing equations, the matching conditions at the fluid/porous interface are automatically satisfied, so that the numerical solution procedure is greatly simplified.

The resulting dimensionless governing equations modified by the artificial compressibility method can be expressed as

$$\frac{\partial W}{\partial t}+\nabla\cdot\vec{F}_{\mathrm{c}}=\nabla\cdot\vec{F}_{\mathrm{v}}+S_{\mathrm{p}}, \tag{1}$$

where

$$W=\begin{bmatrix} p^* \\ \left[\frac{\lambda}{\varepsilon}-(\lambda-1)\right]\vec{U}^* \\ [\lambda(\sigma-1)+1]\vec{T}^* \end{bmatrix},$$

$$\vec{F}_{\mathrm{c}}=\begin{bmatrix} \left[\frac{\lambda}{\varepsilon}-(\lambda-1)\right]\beta\vec{U}^* \\ \left[\frac{\lambda}{\varepsilon^2}-(\lambda-1)\right]\vec{U}^*\vec{U}^*+p^*\delta_{ij} \\ T^*\vec{U}^* \end{bmatrix},$$

$$\vec{F}_{\mathrm{v}}=\begin{bmatrix} 0 \\ \left[\frac{\lambda}{\varepsilon}-(\lambda-1)\right]\frac{1}{Re}\left(\frac{\partial u_i^*}{\partial x_j^*}+\frac{\partial u_j^*}{\partial x_i^*}\right) \\ [\lambda(R_k-1)+1]\frac{1}{PrRe}\nabla T^* \end{bmatrix},$$

$$S_{\mathrm{p}}=\begin{bmatrix} 0 \\ \lambda\left(\frac{1}{DaRe}+\frac{F}{\sqrt{Da}}\left|\vec{U}^*\right|\right)\vec{U}^* \\ 0 \end{bmatrix}.$$

Here W is the vector of dependent variables and $\vec{U}^*$ the velocity vector; $\vec{F}_{\mathrm{c}}$ and $\vec{F}_{\mathrm{v}}$ are the convective flux and viscous flux vector; S_{p} is the source term due to the presence of the porous medium. β is a constant called artificial compressibility whose value affects the solution convergence to steady state. Note that the field variables in the porous region are volume-averaged quantities as described by Vafai and Tien (1981).

The dimensionless variables used in above equations are defined as follows:

$$x^*=\frac{x}{H},\quad y^*=\frac{y}{H},\quad u^*=\frac{u}{u_{\mathrm{av}}},\quad v^*=\frac{v}{u_{\mathrm{av}}},$$

$$t^*=\frac{t}{H/u_{\mathrm{av}}},\quad p^*=\frac{p-p_{\mathrm{o}}}{\rho u_{\mathrm{av}}^2},\quad T^*=\frac{T-T_{\mathrm{i}}}{qH/k},$$

$$\sigma=\frac{(\rho c)_{\mathrm{eff}}}{(\rho c)_{\mathrm{f}}},\quad R_k=\frac{k_{\mathrm{eff}}}{k_{\mathrm{f}}},$$

$$Re=\frac{u_{\mathrm{av}}H}{\nu_{\mathrm{f}}},\quad Pr=\frac{\nu_{\mathrm{f}}}{\alpha_{\mathrm{f}}},\quad Da=\frac{K}{H^2}.$$

As for the flow problem depicted in Fig. 1, no-slip and no-penetration boundary conditions are imposed at the solid walls. At the inlet, fluid has uniform temperature T_{i}, and a fully developed laminar flow profile is prescribed; the downstream end of the computation domain was placed sufficiently far from the step, thus the pressure there can be assumed to be constant. Upper and lower walls are supplied a constant heat flux, while the temperature of step wall is also fixed at T_{i}.

A pair of local Nusselt numbers was evaluated in our study, namely,

$$Nu_{\mathrm{w}}=\frac{qH}{(T_{\mathrm{w}}-T_{\mathrm{b}})k_{\mathrm{f}}}, \tag{2}$$

where T_{b} is the bulk temperature, and

$$Nu=\frac{qH}{(T_{\mathrm{w}}-T_{\mathrm{i}})k_{\mathrm{f}}}. \tag{3}$$

Frictional losses resulting from the porous insert are calculated in terms of the head loss, which can be expressed as

$$h_{\mathrm{l}}=\left(\frac{\bar{p}_{\mathrm{i}}}{\rho_{\mathrm{f}}}+\gamma_{\mathrm{i}}\frac{u_{\mathrm{av,i}}^2}{2}\right)-\left(\frac{\bar{p}_{\mathrm{o}}}{\rho_{\mathrm{f}}}+\gamma_{\mathrm{o}}\frac{u_{\mathrm{av,o}}^2}{2}\right), \tag{4}$$

where $\bar{p}_{\mathrm{i}}$ and $\bar{p}_{\mathrm{o}}$ are the average inlet and outlet pressures, and γ_{i} and γ_{o} are the kinetic energy coefficients (Fox and Mcdonald, 1992).

3. Numerical approach

3.1. Finite-volume method

The 2D equations in (1) are discretized on an unstructured grid. A cell-vertex scheme is adopted here, i.e., all computed variables in vector W are stored at vertices of the triangular cell. For every vertex, as shown in Fig. 2, a control volume is constructed using the median dual of the triangular grid.

Spatial dicretization is performed by using the integral form of the conservation equations over the control volume surrounding node or vertex P,

$$\frac{\partial}{\partial t}\int\int_{S_{\mathrm{cv}}}W_P\,\mathrm{d}S+\int\int_{S_{\mathrm{cv}}}\nabla\cdot\vec{F}_{\mathrm{c}}\,\mathrm{d}S =\int\int_{S_{\mathrm{cv}}}\nabla\cdot\vec{F}_{\mathrm{v}}\,\mathrm{d}S+\int\int_{S_{\mathrm{cv}}}S_{\mathrm{p}}\,\mathrm{d}S. \tag{5}$$

The convection term is transformed in order to introduce the upwind scheme using an edge-based procedure,

$$\int\int_{S_{\mathrm{cv}}}\nabla\cdot\vec{F}_{\mathrm{c}}\,\mathrm{d}S=\oint_{L_{\mathrm{cv}}}\vec{F}_{\mathrm{c}}\cdot\vec{n}\,\mathrm{d}l=\sum_{k=1}^{\mathrm{nedge}}[(\vec{F}_{\mathrm{c}})_{ij}^{k}\cdot\vec{n}\Delta l_k], \tag{6}$$

where nedge is the number of the edges associated with vertex P, $(\vec{F}_{\mathrm{c}})_{ij}^{k}$ is the convection flux through the part of control volume boundary (similar to 1-M_{ij}-2 in Fig. 2) whose length is Δl_k. Therefore, all the fluxes are calculated for the edges and then collected at the two ends of each edge for updating of flow variables in time-marching.

The viscous term is calculated by a cell-based method,

$$\int\int_{S_{\mathrm{cv}}}\nabla\cdot\vec{F}_{\mathrm{v}}\,\mathrm{d}S=\oint_{L_{\mathrm{cv}}}\vec{F}_{\mathrm{v}}\cdot\,\mathrm{d}\vec{l}=\sum_{i=1}^{\mathrm{ncell}}(\vec{F}_{\mathrm{v}}\cdot\Delta\vec{l}_{\mathrm{c}})_i=\frac{1}{2}\sum_{i=1}^{\mathrm{ncell}}(\vec{F}_{\mathrm{v}}\cdot\Delta\vec{l}_{\mathrm{p}})_i,$$

where $\Delta\vec{l}_{ci}$ is the part of control volume boundary in cell C_i, and $\Delta\vec{l}_{\mathrm{p}i}$ is the edge vector of the cell edge opposite to vertex P of the triangle under consideration. Here the $(\vec{F}_{\mathrm{v}})_i$ is calculated at the centre of the triangle cell with a vertex P, which can be obtained by using Green's Theorem based on the variables at the three vertices of the triangle. Similar to the Galerkin type

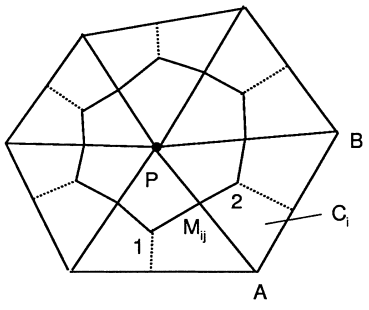

Fig. 2. Construction of the control volume at vertex P.

of formulation, the gradient of a flow variable Φ at the center of a cell is evaluated as

$$\operatorname{grad}\Phi_c = -\frac{1}{2}\frac{\sum_{i=1}^{3}\Phi_i\vec{l}_i}{A},$$

where Φ_i is the flow variable at a vertex i of the cell and $\vec{l}_i$ is the edge vector opposite to vertex i, A is the area of the triangular cell. Gradient at vertices are obtained by a volume averaging of the gradients at the center of cells associated with the vertex under consideration (Zhao and Winterbone, 1995).

3.2. Upwind-biased interpolation

Here an edge-based method of calculating the total inviscid flux is adopted by calculating and storing the flux integrals based on the edges. Such a treatment leads to higher efficiency in computation and reduced data storage requirement.

The left and right state vectors W_L and W_R at a control volume surface are evaluated using the upwind-biased interpolation scheme

$$W_L = W_i + \tfrac{1}{4}[(1-\kappa)\Delta_i^- + (1+\kappa)\Delta_i^+],$$

$$W_R = W_i - \tfrac{1}{4}[(1-\kappa)\Delta_j^+ + (1+\kappa)\Delta_j^-],$$

where

$$\Delta_i^+ = \Delta_j^- = W_j - W_i,$$

$$\Delta_i^- = W_i - W_{i-1} = 2\overrightarrow{ij}\cdot\nabla W_i - (W_j - W_i) = 2\overrightarrow{ij}\cdot\nabla W_i - \Delta_i^+,$$

$$\Delta_j^+ = W_{j+1} - W_j = 2\overrightarrow{ij}\cdot\nabla W_j - (W_j - W_i) = 2\overrightarrow{ij}\cdot\nabla W_j - \Delta_j^-.$$

Therefore

$$W_L = W_i + \tfrac{1}{2}[(1-\kappa)\overrightarrow{ij}\cdot\nabla W_i + \kappa\Delta_i^+],$$

$$W_R = W_j - \tfrac{1}{2}[(1-\kappa)\overrightarrow{ij}\cdot\nabla W_j + \kappa\Delta_j^-],$$

where κ is set to 1/3 which corresponds to a nominally third-order accuracy scheme.

3.3. Upwind characteristics method

The Euler equation modified by Chorin's method are re-written in partial differential form in a Cartesian coordinate system for the derivation of the method of characteristics,

$$\begin{aligned}
&\frac{\partial p}{\partial t} + \beta\frac{\partial u_j}{\partial x_j} = 0,\\
&\frac{\partial u_i}{\partial t} + u_j\frac{\partial u_i}{\partial x_j} + u_i\frac{\partial u_j}{\partial x_j} + \frac{\partial p}{\partial x_i} = 0,\\
&\frac{\partial T}{\partial t} + u_j\frac{\partial T}{\partial x_j} = 0,
\end{aligned} \tag{7}$$

where subscripts i and j equal 1 or 2, representing two spatial coordinates. Suppose that ξ is a new coordinate outward normal to the boundary of a control volume that surrounds a particular vertex. In order to extend the method of characteristics to the unstructured grid solver, it is assumed that flow in ξ direction is approximately one-dimensional and the above equations can then be transformed into

$$\frac{\partial p}{\partial t} + \beta\frac{\partial u_j}{\partial \xi}\xi_{x_j} = 0, \tag{8}$$

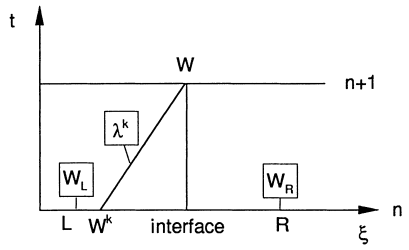

Fig. 3. t–ξ coordinate.

$$\frac{\partial u_i}{\partial t} + u_j\frac{\partial u_i}{\partial \xi}\xi_{x_j} + u_i\frac{\partial u_j}{\partial \xi}\xi_{x_j} + \frac{\partial p}{\partial \xi}\xi_{x_i} = 0, \tag{9}$$

$$\frac{\partial T}{\partial t} + u_j\frac{\partial T}{\partial \xi}\xi_{x_j} = 0, \tag{10}$$

where $\xi_{x_i} = \partial\xi/\partial x_i$ and $\xi_{x_j} = \partial\xi/\partial x_j$.

In the t–ξ space as shown in Fig. 3, flow variable W at time level $n+1$ can be calculated along a characteristics k using a Taylor series expansion and the initial value at time level n (W^k),

$$W = W^k + W_\xi\xi_t\Delta t + W_t\Delta t$$

and

$$W_t = \frac{W - W^k}{\Delta t} - W_\xi\xi_t.$$

A wave speed λ^k is introduced

$$\xi_t = \lambda^k\sqrt{\xi_{x_i}\xi_{x_i}}$$

and the normal vector components are

$$n_{x_j} = \frac{\xi_{x_j}}{\sqrt{\xi_{x_i}\xi_{x_i}}}.$$

Substituting components of W_t into Eqs. (8)–(10), we have

$$\frac{1}{\sqrt{\xi_{x_i}\xi_{x_i}}}\frac{(p-p^k)}{\Delta t} - p_\xi\lambda^k + \beta(u_\xi n_x + v_\xi n_y) = 0, \tag{11}$$

$$\frac{1}{\sqrt{\xi_{x_i}\xi_{x_i}}}\frac{(u-u^k)}{\Delta t} - u_\xi(\lambda^0 - \lambda^k) + u(u_\xi n_x + v_\xi n_y) + p_\xi n_x = 0, \tag{12}$$

$$\frac{1}{\sqrt{\xi_{x_i}\xi_{x_i}}}\frac{(v-v^k)}{\Delta t} - v_\xi(\lambda^0 - \lambda^k) + v(u_\xi n_x + v_\xi n_y) + p_\xi n_y = 0, \tag{13}$$

$$\frac{1}{\sqrt{\xi_{x_i}\xi_{x_i}}}\frac{(T-T^k)}{\Delta t} - T_\xi(\lambda^0 - \lambda^k) = 0, \tag{14}$$

where λ^0 is the contra-variant velocity

$$\lambda^0 = un_x + vn_y.$$

In order to derive the compatibility equations, the spatial derivatives, such as u_ξ, v_ξ, p_ξ and T_ξ have to be eliminated from the above equations. Following the approach of Eberle (1985) for compressible flow equations, each of the above four equations is multiplied by an arbitrary variable and all the resulting equations are summed to form a new equation

$$\frac{1}{\Delta t\sqrt{\xi_{x_i}\xi_{x_i}}}A - p_\xi B + u_\xi C + v_\xi D + T_\xi E = 0, \tag{15}$$

where

$$A = a(p - p^k) + b(u - u^k) + c(v - v^k) + d(T - T^k),$$
$$B = -a\lambda^k + bn_x + cn_y,$$
$$C = an_x\beta + b(\lambda^0 - \lambda^k + un_x) + cvn_x,$$
$$D = an_y\beta + bun_y + c(\lambda^0 - \lambda^k + vn_y),$$
$$E = d(\lambda^0 - \lambda^k)$$

and a, b, c and d are the arbitrary variables used to multiply the equations. We define the coefficients of the partial space derivatives to be zero, i.e., A, B, C, D and E are zero,

$$A = 0, \tag{16}$$

$$B = 0, \tag{17}$$

$$C = 0, \tag{18}$$

$$D = 0, \tag{19}$$

$$E = 0. \tag{20}$$

Eqs. (16)–(21) constitute a linear system $\Phi X = 0$ with $X = \{a, b, c, d\}$. Variables a, b, c and d are generally non-zero, thus the system of equations has non-trivial solution. This means that $\det(\Phi) = 0$, and the following eigenvalues can be derived as

$$\lambda_1 = \lambda_2 = \lambda^0,$$
$$\lambda_3 = \lambda^1 = \lambda^0 + \sqrt{(\lambda^0)^2 + \beta},$$
$$\lambda_4 = \lambda^2 = \lambda^0 - \sqrt{(\lambda^0)^2 + \beta}.$$

For each eigenvalue or characteristics speed, characteristic equations can be derived from Eqs. (16)–(20). For example, for $\lambda^k = \lambda^0$, we have

$$a = \frac{bn_x + cn_y}{\lambda^0}.$$

Substituting this into Eq. (16), we obtain

$$\frac{bn_x + cn_y}{\lambda^0}(p - p^0) + b(u - u^0) + c(v - v^0) + d(T - T^0) = 0,$$

i.e.,

$$b[n_x(p - p^0) + \lambda^0(u - u^0)] + c[n_y(p - p^0) + \lambda^0(v - v^0)] + d\lambda^0(T - T^0) = 0.$$

For any b, c and d, the above equation is always satisfied. Therefore all the terms in square brackets are zero. As a result, we have

$$(u - u^0)n_y - (v - v^0)n_x = 0, \tag{21}$$

$$T = T^0. \tag{22}$$

For $\lambda = \lambda^1$

$$p - p^1 = -\lambda^1[(u - u^1)n_x + (v - v^1)n_y]. \tag{23}$$

For $\lambda = \lambda^2$

$$p - p^2 = -\lambda^2[(u - u^2)n_x + (v - v^2)n_y]. \tag{24}$$

Finally, all the variables are determined using the above characteristics equations (21)–(24):

$$u = fn_x + u^0n_y^2 - v^0n_xn_y,$$

$$v = fn_y + v^0n_x^2 - u^0n_yn_x,$$

$$p = p^1 - \lambda^1[(u - u^1)n_x + (v - v^1)n_y]$$

or

$$p = p^2 - \lambda^2[(u - u^2)n_x + (v - v^2)n_y],$$

where

$$f = \frac{1}{2C}[p^1 - p^2 + n_x(\lambda^1u^1 - \lambda^2u^2) + n_y(\lambda^1v^1 - \lambda^2v^2)],$$
$$C = \sqrt{(\lambda^0)^2 + \beta}.$$

Flow quantities at time level $n + 1$ obtained from the above equations on the characteristics are then used to calculate convection fluxes at the control volume interface, while those on different characteristics at time level n are approximately evaluated by an upwind scheme using the signs of the characteristics as suggested by Drikakis et al. (1994),

$$W^j = \tfrac{1}{2}[(1 + \mathrm{sign}(\lambda^j))W_\mathrm{L} + (1 - \mathrm{sign}(\lambda^j))W_\mathrm{R}],$$

where W_L and W_R are obtained by the upwind-biased interpolation.

3.4. Time integration

Finally, for a certain vertex P, the spatially discretized equations form a system of coupled ordinary differential equations, which may be written as

$$\frac{\partial}{\partial t}(W_\mathrm{p}) = -\frac{1}{\Delta S_\mathrm{cv}}\left\{\sum_{k=1}^{\mathrm{nedge}}[(\vec{F}_\mathrm{c})_{ij}^k \cdot \vec{n}\Delta l_k)] - \frac{1}{2}\sum_{i=1}^{\mathrm{ncell}}(\vec{F}_\mathrm{c} \cdot \vec{n}\Delta l_P)_i\right\} + S_\mathrm{p}$$
$$= -\frac{1}{\Delta S_\mathrm{cv}}Q(W_P) + S_\mathrm{p} = -R(W_P), \tag{25}$$

where the right-hand side represents the residual error, or deviation from steady state.

The steady state solution is reached by integration in time of the above equation. This is performed using an explicit Runge–Kutta scheme. To advance the solution in time from n to $n + 1$, the general formulation of a m-stage Runge–Kutta scheme is

$$W_P^{(0)} = W_P^n,$$
$$W_P^{(1)} = W_P^{(0)} - \alpha_1\Delta tR(W_P^{(0)}),$$
$$\vdots$$
$$W_P^{(m-1)} = W_P^{(0)} - \alpha_{m-1}\Delta tR(W_P^{(m-2)}),$$
$$W_P^{(m)} = W_P^{(0)} - \alpha_m\Delta tR(W_P^{(m-1)}),$$
$$W_P^{n+1} = W_P^{(m)},$$

where the coefficients α_j, $j = 1, m$ are the standard weights of the Runge–Kutta time integration. A five-stage scheme is used in this study.

The local time step size is estimated via CFL stability condition

$$\Delta t = \mathrm{CFL} \cdot \frac{\Delta l}{\mathrm{Max}(\lambda^j)}, \quad j = 0, 1, 2.$$

Here Δl is the length scale associated with a node under consideration. Normally, it is taken as the smallest height of all the cells sharing the node.

3.5. Convergence acceleration techniques

3.5.1. Point-implicit treatment to the source terms

It has been found that the explicit solutions of the spatially discretized Eq. (25) might encounter low convergence rate and

even instability problems caused by the source terms in the governing equations. Therefore, a point-implicit treatment is introduced for the source terms in the governing equations. This can be expressed as

$$\frac{\partial W_P}{\partial t} = -\frac{Q(W_P)}{\Delta S_{cv}} + S_p^{n+1}. \tag{26}$$

Here, the source S_p is treated implicitly by using the Taylor expansion. S_p at the time step $n+1$ can be evaluated as

$$S_p^{n+1} = S_p^n + \frac{\partial S_p}{\partial W_P}\frac{\partial W_P}{\partial t}\Delta t.$$

Then, Eq. (26) becomes

$$\frac{\partial W_P}{\partial t} = \frac{R(W_P)}{\left(1 - \Delta t(\partial S_p/\partial W_P)\right)}, \tag{27}$$

where $R(W_P) = -(Q(W_P)/\Delta S_{cv}) + S_p^n$, and $\partial S_p/\partial W_P$ can be easily obtained.

Numerical tests showed that the present treatment is very effective in obtaining convergent solutions.

3.5.2. Implicit residual smoothing

The idea behind this is to replace the residual at one point of a flow field with a smoothed or weighted average of the residuals at the neighboring points. The averaged residuals are calculated implicitly in order to increase the maximum CFL number, thus increase the convergence rate. Normally this procedure allows the CFL number to be increased by a factor of 2 or 3. The smoothing equation for a vertex k can be expressed as

$$\bar{R}_k = R_k + \varphi\delta^2\bar{R}_k, \tag{28}$$

where R is the original residual, $\bar{R}$ is smoothed residual and ε is the smoothing coefficient,

$$\varphi = \max\left\{\frac{1}{4}\left[\left(\frac{\mathrm{CFL}}{\mathrm{CFL}^*}\right)^2 - 1\right],\ 0\right\}, \tag{29}$$

where CFL^* is the maximum CFL number of the basic scheme. The solution to the above equations can be obtained on an unstructured grid by a Jacobi iterative method

$$\bar{R}_k^{(m)} = R_k^{(0)} + \varphi\sum_{i=1}^{\mathrm{numnod}(k)}[\bar{R}_i^{(m)} - \bar{R}_k^{(m)}],$$

i.e.,

$$\bar{R}_k^{(m)} = \frac{R_k^{(0)} + \varphi\sum_{i=1}^{\mathrm{numnod}(k)}\bar{R}_i^{(m-1,m)}}{1 + \varepsilon\,\mathrm{numnod}(k)}, \tag{30}$$

where $\mathrm{numnod}(k)$ is the number of neighbouring nodes of vertex k.

4. Results and discussion

The use of porous inserts for heat transfer enhancement in the flow over a backward-facing step has been firstly investigated by Martin et al. (1998). In their study, the porous inserts consist of square arrays of fibres mounted transverse to the streamwise flow with highly conducting silicon carbide selected as the fibre material. Since the heat transfer improvements in this flow system is mainly owing to the changes in the nature of downstream flow field, it is not necessary to use highly conducting porous inserts in obtaining comparable enhancement. Hence, in the present study, the conductivity of the porous medium was taken to be equal to that of the fluid, so that the effects of conduction within the solid matrix could be eliminated. An isotropic high-porosity insert made of foam material was selected, and the typical values of physical parameters used in this study were: $Re = 800$, $Pr = 0.72$ and $F = 0.1$. The parameter studies were concentrated on the effects of Darcy number and the length of porous insert on the fluid flow and heat transfer performance in the channel.

Referring to Fig. 1, the flow field was solved by the finite-volume method over a non-uniform triangular mesh with a large concentration of nodes in regions of high gradients, such as those close to the walls and the corner of the step. A mesh which has 17,239 nodes and 33,111 triangular cells was employed. No more than 1% difference in results is found when mesh density is further increased. The downstream channel length was taken as 15 times channel height, i.e. 30 times step height, such that the outflow boundary is far enough from the step and its effects on the flow and heat transfer in the upstream region of the channel are negligible.

The validity of the numerical scheme was verified by comparing with relevant results reported in the literature. The basic characteristics of the backward-facing step flow at $Re = 800$ is illustrated in the streamline plot of Fig. 4(a), where two separation zones exist in the channel. The results of this study are also compared quantitatively with those obtained by Gartling (1990) and Martin et al. (1998) as shown in Fig. 4(b) and (c). Results for fully developed flow in a fully porous channel with constant heat flux at the walls were compared with the analytical solutions reported by Lauriat and Vafai (1991) and Vafai and Kim (1989) (see Fig. 5). It should be noted that

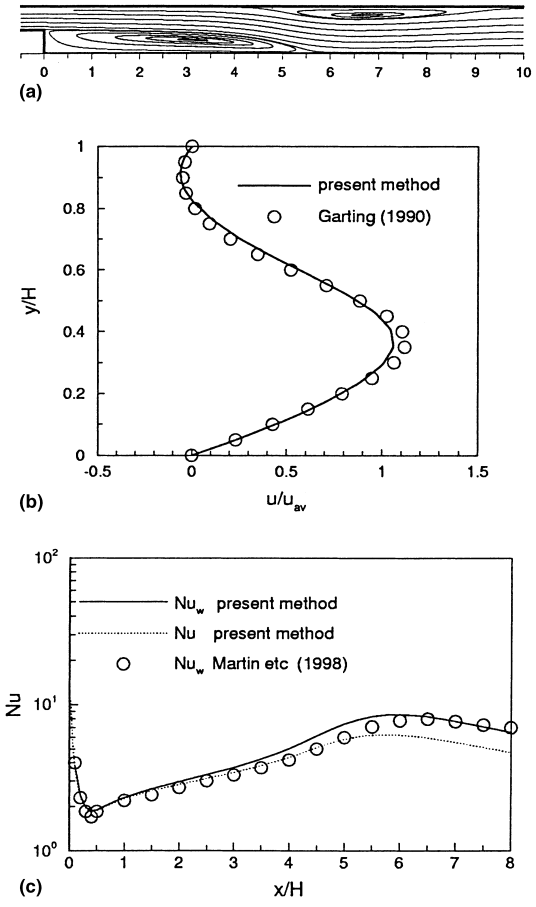

Fig. 4. Backward-facing step flow at $Re = 800$: (a) streamline plot; (b) streamwise velocity profile at $x/H = 7$; (c) lower wall Nusselt number versus axial location.

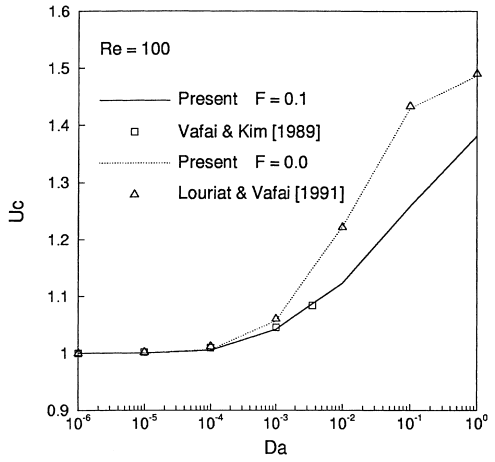

Fig. 5. Comparison of fully developed centreline velocity.

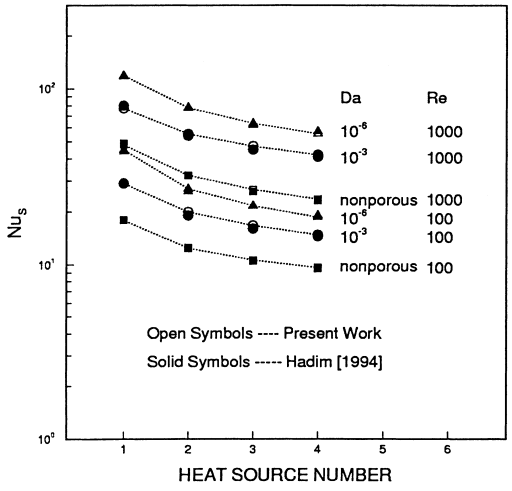

Fig. 6. Variation of Nusselt number averaged over each heat source.

Vafai and Kim's solution is valid up to $Da = 1$ when inertial effects are included. As for the case of flow over a composite porous/fluid system, systematic validation was conducted by comparing the heat transfer results with those obtained by Hadim (1994) for forced convection in a partially porous channel with discrete heat sources (Fig. 6). Good agreement can be found in these comparisons, thus verifying the methods proposed.

4.1. Hydrodynamic results

It is believed that the presence of porous inserts can change the characteristics of a flow field significantly. The influence of the porous matrix inserts on the downstream flow is clearly shown in Figs. 7–9 for $Da = 1 \times 10^{-2}$, 1×10^{-3} and 1×10^{-4}. Note that the flow field in the first 20 step heights of the channel are presented only. Referring to Fig. 7 for the case of highest Darcy number considered, the flow field is similar to the homogeneous case when $a/H = 0.1$ (Fig. 4(a)), but both the primary recirculation zone along the lower wall and the secondary recirculation zone along the upper wall are shortened. However, no lengthening of the lower wall recirculation zone is observed as reported by Martin et al. (1998). Further increasing a/H, the size of lower wall recirculation zone is successively reduced, and the upper wall recirculation zone has

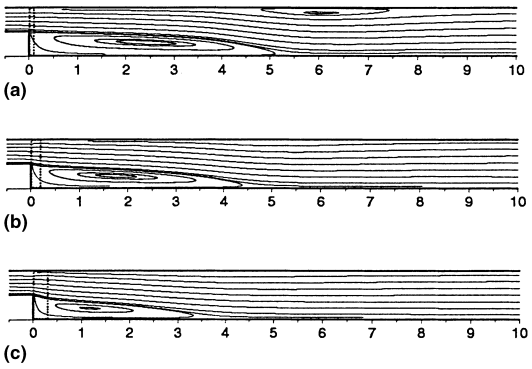

Fig. 7. Streamline plots for $Da = 1 \times 10^{-2}$: (a) $a/H = 0.1$; (b) $a/H = 0.2$; (c) $a/H = 0.3$.

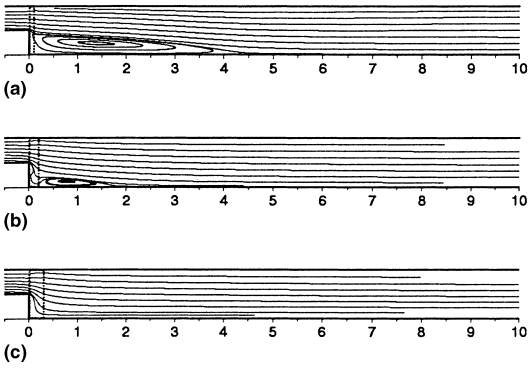

Fig. 8. Streamline plots for $Da = 1 \times 10^{-3}$: (a) $a/H = 0.1$; (b) $a/H = 0.2$; (c) $a/H = 0.3$.

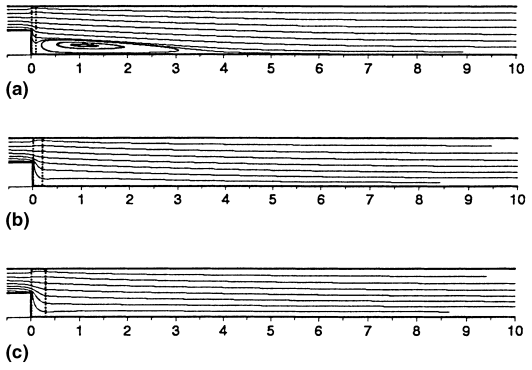

Fig. 9. Streamline plots for $Da = 1 \times 10^{-4}$: (a) $a/H = 0.1$; (b) $a/H = 0.2$; (c) $a/H = 0.3$.

been eliminated. When Darcy number is decreased, as shown in Figs. 8 and 9, the lower wall recirculation zone is reduced in size faster and eventually disappears at higher a/H value. In addition, the upper wall separation can not be seen even with the shortest insert. These changes of downstream flow structure in the channel are owing to the bulk damping by the presence of porous insert. As the fluid moves from the inlet through the porous insert, the strong resistance causes the streamwise velocity profile to be flattened, hence the flow separation behind the step is greatly damped. The bulk resistance to flow is increased as Darcy number decreases, the recirculation zone is finally eliminated if porous insert is long enough.

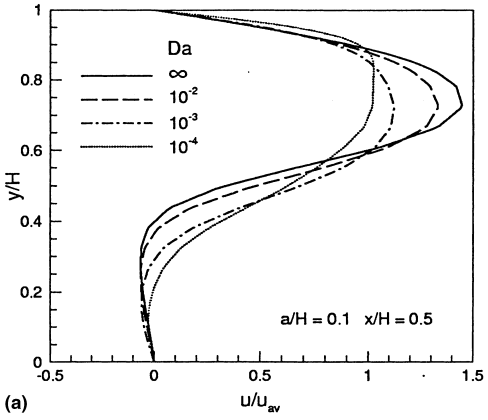

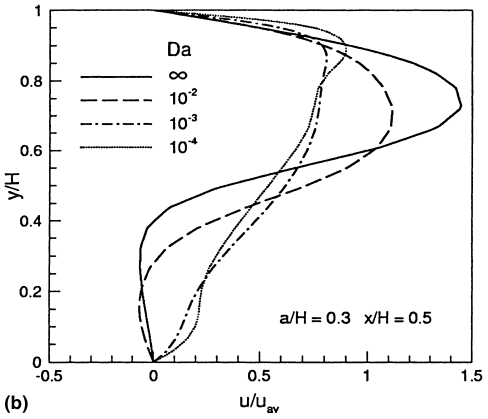

Fig. 10. Streamwise velocity profiles at $x/H = 0.5$: (a) $a/H = 0.1$; (b) $a/H = 0.3$.

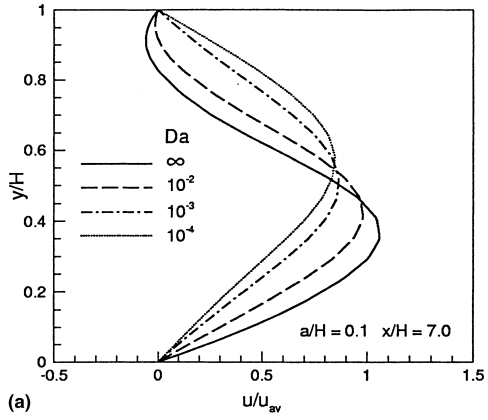

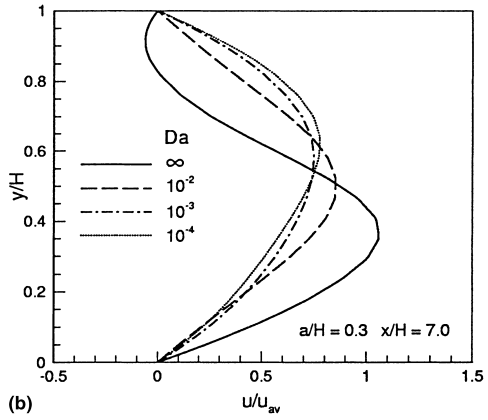

Fig. 11. Streamwise velocity profiles at $x/H = 7.0$: (a) $a/H = 0.1$; (b) $a/H = 0.3$.

The flattening of velocity profiles due to the porous inserts can be seen in Fig. 10, where u velocity profiles at the location of one step height downstream of the step for $a/H = 0.1$ and 0.3 is displayed. As expected, the deviation from the homogeneous case is more evident with a decrease in Darcy number and/or an increase in length of the porous inserts. Large deviations in velocity profile are also found at a downstream location of $x/H = 7$ (Fig. 11), since the upper wall separation usually no longer exists in the presence of porous inserts.

When a porous insert is used for heat transfer enhancement in the channel, the penalty arising from increased frictional loss must be considered carefully. The dimensionless channel head loss (normalized by the homogeneous value) is displayed in Fig. 12 as a function of insert length for different Darcy numbers. It is found that friction losses resulting from porous inserts rise almost linearly with insert length. A substantially increase in frictional loss is observed as the Darcy number is decreased. The minimum head loss for eliminating the recirculation zone is about three and half times the no-insert value, with a combination of $a/H = 0.3$ and $Da = 1 \times 10^{-3}$.

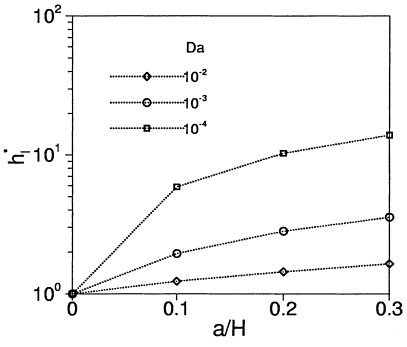

Fig. 12. Dimensionless channel head loss.

4.2. Heat transfer results

It is reasonable to expect that the change in the nature of flow field due to porous insert would greatly affect the temperature distributions at channel walls. The lower wall temperature, normalized by the maximum wall temperature for the homogeneous case, is illustrated in Fig. 13 as a function of axial location for three Darcy numbers. For the homogeneous case, the wall temperature peaks near the upstream edge of recirculation zone, and reaches a local minimum value after reattachment. When porous inserts are added, the maximum value of wall temperature is reduced with increase in a/H and/or decrease in Darcy number, and eventually disappears for a combination of insert length and Darcy number. These trends are directly related to the length reducing or elimination of recirculation zone behind the step. It have been found that more than 40% reduction in local maximum temperature can be achieved after flow separation is eliminated by the presence of porous inserts.

The results presented so far suggest that the addition of porous insert could improve the heat transfer performance of the studied problem. This is more clearly shown in Fig. 14, where the axial distributions of the lower wall Nusselt number for various combinations of insert length and Darcy number are illustrated. As expected, the heat transfer enhancement is

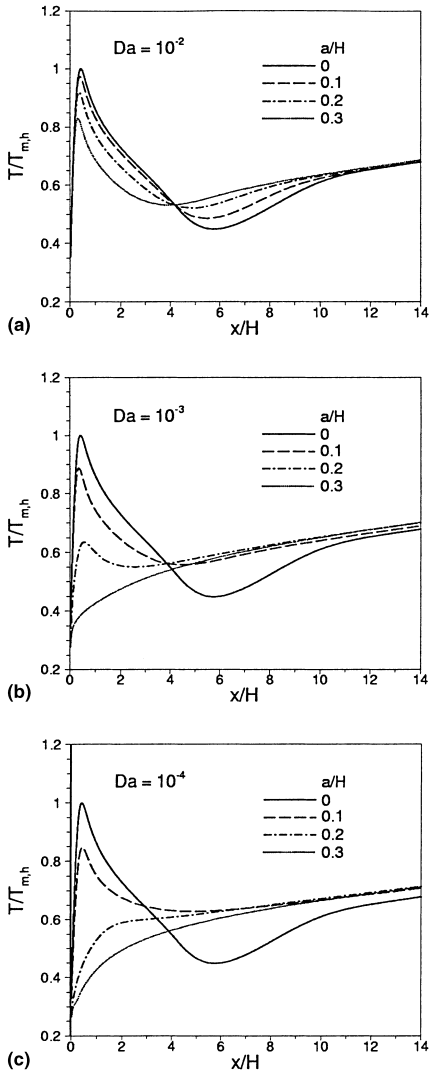

Fig. 13. Axial distributions of lower wall temperature: (a) $Da = 1 \times 10^{-2}$; (b) $Da = 1 \times 10^{-3}$; (c) $Da = 1 \times 10^{-4}$.

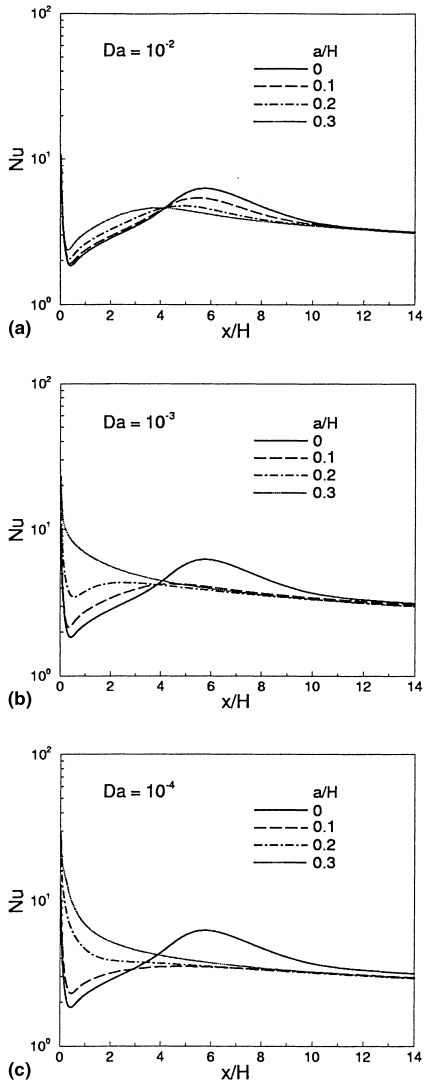

Fig. 14. Axial distributions of lower wall Nusselt number: (a) $Da = 1 \times 10^{-2}$; (b) $Da = 1 \times 10^{-3}$; (c) $Da = 1 \times 10^{-4}$.

more pronounced for the cases of lower Darcy number and longer insert. In view of minimizing the frictional losses resulting from the porous insert, the combination of a medium Darcy number and long insert is favored.

It should be noted that the ratio of the effective thermal conductivity of porous medium to fluid conductivity was set only equal to 1 in this study, and heat transfer is expected to be further enhanced with a high-conductivity porous insert.

5. Concluding remarks

A new high-order upwind characteristics finite-volume algorithm for numerical simulation of incompressible laminar flow and forced convection heat transfer over a fluid/porous composite system has been presented. The use of unstructured approaches make the scheme very flexible in dealing with complex boundary geometry. The introduction of unified governing equations greatly simplified the numerical solution procedure for the flow over a composite system, since no matching conditions at the fluid/porous interface are needed. The discretized equations are solved by an explicit multistage Runge–Kutta time stepping scheme. It has been proved that the point-implicit treatment to porous-insert-introduced source terms in discretized equations is very effective in obtaining converged solution. The numerical model has been validated through a number of test cases. The results of numerical investigation on fluid flow over a 2D backward-facing step showed that the porous insert influences the downstream flow structure greatly, the heat transfer performance is hence improved significantly even if the thermal conductivity of porous medium is the same as the fluid.

Acknowledgements

Financial support by the National Science and Technology Board (Singapore) in the project of Micro Cooling Technology for Electronics System is gratefully acknowledged.

References

Abu-Hijleh, B., 1997. Convection heat transfer from a laminar flow over a 2-D backward facing step with asymmetric and orthotropic porous floor segments. Numer. Heat Transfer A 31, 325–335.

Chorin, A., 1967. A numerical method for solving incompressible viscous flow problems. J. Comput. Phys. 2, 12–26.

Drikakis, D., Govatsos, P.A., Papantonis, D.E., 1994. A characteric-tic-based method for incompressible flows. Int. J. Numer. Meth. Fluids 19, 667–685.

Eberle, A., 1985. 3D Euler calculations using characteristics flux extrapolation. AIAA-85-0119.

Fox, R.W., McDonald, A.T., 1992. Introduction to Fluid Mechanics, fourth ed. Wiley, New York, pp. 328–330.

Fu, W.-S., Huang, H.-C., Liou, W.-Y., 1996. Thermal enhancement in Laminar channel flow with a porous block. Int. J. Heat Mass Transfer 39 (10), 2165–2175.

Gartling, D.K., 1990. A test problem for outflow boundary conditions flow over a backward-facing step. Int. J. Numer. Meth. Fluids 11, 953–967.

Hadim, A., 1994. Forced convection in a porous channel with localized heat sources. J. Heat Transfer 116, 465–472.

Huang, P.C., Vafai, K., 1994. Analysis of forced convection enhancement in a channel using porous blocks. J. Thermophys. Heat Transfer 8 (3), 563–573.

Lauriat, G., Vafai, K., 1991. Forced convection and heat transfer through a porous medium exposed to a flat plate or a channel. In: Convective Heat and Mass Transfer in Porous Media. Kluwer Academic, Dordrecht, pp. 289–327.

Martin, A.R., Satiel, C., Shyy, W., 1998. Heat transfer enhancement with porous inserts in recirculating flow. J. Heat Transfer 120, 458–467.

Patankar, S.V., 1980. Numerical Heat Transfer and Fluid Flow. Hemisphere, New York.

Vafai, K., Kim, S.J., 1989. Forced convection in a channel filled with a porous medium: an exact solution. J. Heat Transfer 111, 1103–1106.

Vafai, K., Tien, C.L., 1981. Boundary and inertial effects on flow and heat transfer in porous media. Int. J. Heat Mass Transfer 24, 195–203.

Zhao, Y., Winterbone, D.E., 1995. The finite volume FLIC method and its stability analysis. Int. J. Mech. Sci. 37, 1147–1160.